Acta Crystallographica Section A
Foundations and Advances
ISSN 2053-2733

Received 29 January 2014
Accepted 10 April 2014

© 2014 International Union of Crystallography

Multiple Bragg reflection by a thick mosaic crystal

Joachim Wuttke

Forschungszentrum Jülich GmbH, Jülich Centre for Neutron Science at MLZ, Lichtenbergstrasse 1, D-85747 Garching, Germany. Correspondence e-mail: j.wuttke@fz-juelich.de

Symmetric Bragg-case reflections from a thick, ideally imperfect, crystal slab are studied mostly by analytical means. The scattering transfer function of a thin mosaic layer is derived and brought into a form that allows for analytical approximations or easy quadrature. The Darwin–Hamilton equations are generalized, lifting the restriction of wavevectors to a two-dimensional scattering plane. A multireflection expansion shows that wavevector diffusion can be studied independently of the real-space coordinate. Combining analytical arguments and Monte Carlo simulations, multiple Bragg reflections are found to result in a minor correction of the reflected intensity, a moderate broadening of the reflected azimuth angle distribution, a considerable modification of the polar angle distribution, and a noticeable shift and distortion of rocking curves.

1. Introduction

Purposely imperfect crystals have important applications in neutron and X-ray optics. However, the available literature, reviewed in *International Tables for Crystallography* (Sabine, 2004), seems to be mostly concerned with extinction corrections required in crystallographic studies of imperfect specimens, and less with their uses as optical elements. The established theory provides no adequate foundation for computing the directional distribution of radiation deflected by a thick mosaic crystal. This limits for instance the reliability of simulations (Meyer *et al.*, 2003; Hennig *et al.*, 2011) of a phase-space transforming rotating beam deflector for third-generation neutron backscattering spectrometers (Schelten & Alefeld, 1984; Meyer *et al.*, 2003; Wuttke *et al.*, 2012).

Following Darwin (1922), a mosaic crystal is modelled as an assembly of perfectly crystalline blocks that are to some degree orientationally disordered. In an ideally imperfect crystal, every block is so thin that it reflects at most a small fraction of the incident beam. Therefore, primary extinction and all kind of quantum effects arising from coherent superposition of multiple reflections within a block can be neglected. Here we consider a thick, ideally imperfect, crystal, consisting of so many block layers that secondary extinction and multiple reflections between blocks are of practical importance. To arrive at specific conclusions, we consider a slab with surface normal along the average block normal, we only study 'Bragg' reflection geometry (as opposed to the 'Laue' deflected-transmission case), and we exclude grazing incidence and near backscattering.

Since reflections from different blocks add incoherently, they can be treated by classical transport theory. This is usually done in form of the Darwin–Hamilton equations (Hamilton, 1957):

$$\hat{\mathbf{k}}_{\pm}\nabla I_{\pm} = \mu I_{\mp} - \nu I_{\pm}, \tag{1}$$

where $\hat{\mathbf{k}}_{\pm}$ are the directions of the incident and diffracted beam and $I_{\pm}$ are the corresponding currents. The lineic reflectivity μ accounts for gains by Bragg scattering; the attenuation coefficient $\nu = \mu + \sigma_{\rm abs} + \sigma_{\rm inel} + \sigma_{\rm diff}$ accounts for losses by Bragg scattering, by absorption, by inelastic scattering and by diffuse scattering. Werner (1974) has formally solved the equations (1) for a parallelepiped. Sears (1997) has obtained a practicable closed expression for a slab. Solutions for $\nu = \mu$ have been known for a long time (Bacon & Lowde, 1948).

The Bragg reflectivity μ depends on the distribution W of block orientations and on the blocks' shape transform Σ. Excluding excessively thin blocks from further consideration, we can assume Σ to be a much narrower bandpass than W. The reflectivity then depends only on W, not on Σ:

$$\mu = \bar{\mu} W\big(\theta - \theta_{\rm B}\big), \tag{2}$$

where θ is the incident glancing angle and $\theta_{\rm B}$ is the Bragg angle of an untilted crystallite (Zachariasen, 1945, equation 4.19; Sears, 1989, equation 5.2.70).

Implicitly, the Darwin–Hamilton equations confine block normals and wavevectors to a fixed scattering plane. Only in this approximation the diffracted beam direction is unique. In reality, for a given incoming wavevector, the Bragg condition is fulfilled by a pencil of block orientations, and the diffracted beam is spread accordingly into a pencil of rays. From the second reflection onwards, the wavevectors form a two-dimensional manifold. As pointed out by Werner (1974), this was fully appreciated by Darwin (1922, p. 818): 'The problem of these multiple reflections would be exceedingly difficult if it were treated exactly: for each layer will, on account of

diffraction, spread out incident parallel rays into a certain range of angles and so will continuously change the angle at which they attack successive layers.'

Unafraid of what seemed exceedingly difficult almost a century ago, this paper presents a thorough investigation of the angular spread of multiply diffracted rays. The initial idea was to solve the problem by Monte Carlo simulation, a method that was not available for Darwin, but has long since become standard for the study of radiation transport (*e.g.* Spanier & Gelbard, 1969). However, in setting up the simulation it became necessary to investigate the peculiar kernel of the transport equation by analytical means, and in the end, a coherent picture emerged with only a little need for complementary simulations.

In the following, we first assemble a formalism for Bragg reflections by a thin mosaic layer and investigate analytical approximations (§2). We then derive generalized Darwin–Hamilton equations and study them analytically (§3). Monte Carlo integration is outlined briefly (§4). In conclusion, we can say how out-of-plane scattering affects reflectivity of a thick mosaic and how the wavevector distribution broadens (§5).

2. Reflectivity of a thin mosaic layer

As a foundation for the following investigation of a thick mosaic crystal, we need to derive the Bragg reflectivity of a thin mosaic layer. In the following, we first review the reflectivity of a single block (§2.1). We then average over block orientations (§2.2) and introduce a few restrictions, assumptions and approximations to settle on a transfer function that constitutes a simple, yet realistic, mathematical model of a mosaic crystal (§2.3). We then discuss some analytical approximations (§2.4) and test them numerically (§2.5).

2.1. Transfer function of a crystalline block

Crystalline blocks are required to be so thin that we can work in kinematical approximation, neglecting multiple scattering within blocks. The orientation of a block shall be indicated by the normal vector $\hat{\mathbf{u}}$, as shown in Fig. 1. The double differential cross section, normalized to the block volume V, can then be written as a transfer function

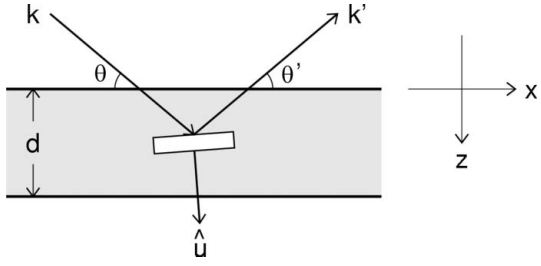

Figure 1
Geometry for a single Bragg reflection by a crystalline block within a mosaic crystal shaped as a slab of thickness d. While the incoming wavevector $\mathbf{k}$ is chosen to lie in the xz plane, the block orientation $\hat{\mathbf{u}}$ and the outgoing wavevector $\mathbf{k}'$ may also have y components. The angle θ' is not in the drawing plane unless $\mathbf{k}'$ is.

$$\mu_{\hat{\mathbf{u}}}(\mathbf{k}', \mathbf{k}) = \frac{1}{Vk'^2}\frac{\partial^2\sigma}{\partial\Omega\partial k'}, \tag{3}$$

i.e. the probability per unit length that a particle with incoming wavevector $\mathbf{k}$ is scattered into an infinitesimal phase-space volume d^3k' around $\mathbf{k}'$.

In the following, we only consider elastic scattering:

$$\frac{\partial^2\sigma}{\partial\Omega\partial k'} = \frac{\partial\sigma}{\partial\Omega}\,\delta(k'-k) + \text{losses}. \tag{4}$$

The losses by inelastic scattering are comprised in the attenuation coefficient ν as introduced in (1), and will therefore be ignored in the following. The delta function ensures energy conservation.

We assume that there is exactly one possible Bragg reflection, given by

$$\mathbf{k}' = \mathbf{k} \mp 2\tau\hat{\mathbf{u}}, \tag{5}$$

where τ is a material constant, and the factor two is chosen for later convenience. The double sign has the same meaning as in the Darwin–Hamilton equations (1): the upper sign holds for the geometry shown in Fig. 1 and more generally for each second reflection in a multiple-reflection series.

The differential cross section for elastic coherent scattering (Sears, 1989, equations 5.2.18) now takes the form

$$\frac{\partial\sigma}{\partial\Omega} = V\frac{(2\pi)^3}{V_\mathrm{u}^2}|F|^2\,\Sigma\big(\mathbf{k}' - \mathbf{k} \pm 2\tau\hat{\mathbf{u}}\big). \tag{6}$$

The unit-cell volume V_u and the unit-cell structure factor $|F|^2$ (which includes the Debye–Waller factor) shall be lumped into a material constant with the dimension of a wavenumber,

$$P := \left[\frac{(2\pi)^3|F|^2}{V_\mathrm{u}^2}\right]^{1/4}. \tag{7}$$

Equation (6) further contains the squared modulus of the crystallite shape transform (Sears, 1989, equations 5.1.10,12)

$$\Sigma(\boldsymbol{\kappa}) := \frac{1}{V(2\pi)^3}\left|\int_V \mathrm{d}^3r\exp(i\boldsymbol{\kappa}\mathbf{r})\right|^2, \tag{8}$$

which is a very narrow bandpass except for very thin crystallites. In the following, we approximate it as

$$\Sigma(\boldsymbol{\kappa}) \doteq \delta^3(\boldsymbol{\kappa}). \tag{9}$$

The superscript three emphasizes that this delta function has a vectorial argument, as opposed to the delta function of a scalar argument in (4).

To summarize, the reflectivity of a crystalline block is governed by the transfer function

$$\mu_{\hat{\mathbf{u}}}\big(\mathbf{k}', \mathbf{k}\big) = \frac{P^4}{k^2}\,\delta^3\big(\mathbf{k}' - \mathbf{k} \pm 2\tau\hat{\mathbf{u}}\big)\,\delta\big(k' - k\big). \tag{10}$$

In the context set by the two delta functions, we are allowed to equate

$$k' - k = \frac{k'^2 - k^2}{2k} = \frac{\big(\mathbf{k} \mp 2\tau\hat{\mathbf{u}}\big)^2 - k^2}{2k} = \frac{2\tau}{k}\big(\tau \mp \mathbf{k}\hat{\mathbf{u}}\big), \tag{11}$$

so that (10) becomes

$$\mu_{\hat{\mathbf{u}}}(\mathbf{k}', \mathbf{k}) = \frac{P^4}{2k\tau}\delta^3\big(\mathbf{k}' - \mathbf{k} \pm 2\tau\hat{\mathbf{u}}\big)\delta\big(\mathbf{k}\hat{\mathbf{u}} \mp \tau\big). \tag{12}$$

2.2. Orientational average

The transfer function of a thin mosaic layer is obtained by averaging (12) over block orientations,

$$\mu(\mathbf{k}', \mathbf{k}) := \int \mathrm{d}^2\hat{u} W\big(\hat{\mathbf{u}}\big)\mu_{\hat{\mathbf{u}}}\big(\mathbf{k}', \mathbf{k}\big). \tag{13}$$

The integral runs over the unit sphere. The second delta function in (12) restricts the contributing $\hat{\mathbf{u}}$ to a plane. The intersection of the unit sphere and the plane is a circle. In the following, we work out an explicit expression for (13) as a line integral along this circle.

From this point on, we work in the specific coordinate system introduced in Fig. 1. We also need the polar coordinates of the incoming wavevector,

$$\mathbf{k} = k\begin{pmatrix} \cos\theta_{\mathbf{k}}\cos\varphi_{\mathbf{k}} \\ \cos\theta_{\mathbf{k}}\sin\varphi_{\mathbf{k}} \\ \pm\sin\theta_{\mathbf{k}} \end{pmatrix}. \tag{14}$$

We set up a rotation matrix

$$R_{\mathbf{k}} := R(\varphi_{\mathbf{k}}) := \begin{pmatrix} \cos\varphi_{\mathbf{k}} & -\sin\varphi_{\mathbf{k}} & 0 \\ \sin\varphi_{\mathbf{k}} & \cos\varphi_{\mathbf{k}} & 0 \\ 0 & 0 & 1 \end{pmatrix}, \tag{15}$$

so that $R_{\mathbf{k}}^{-1}\mathbf{k}$ lies in the xz plane. We parameterize the rotated block normal

$$\hat{\mathbf{v}} := R_{\mathbf{k}}^{-1}\hat{\mathbf{u}} \tag{16}$$

by its orthographic projection into the xy plane:

$$\hat{\mathbf{v}}(\alpha, \beta) = \Big(\alpha, \beta, \sqrt{1 - \alpha^2 - \beta^2}\Big). \tag{17}$$

We will make sustained use of the assumption that the mosaic is highly ordered so that $W(\hat{\mathbf{u}})$ takes substantially nonzero values only in a small subregion of the unit sphere. This region is centred at $\langle\hat{\mathbf{u}}\rangle = \hat{\mathbf{z}}$ and it has a diameter of a few η, which is small compared with one. This justifies the parameterization (17) as fully sufficient to cover the relevant part of the unit sphere. Throughout this paper we exclude grazing incidence, requesting $\theta \gg \eta$, so that even and odd reflection orders remain strictly separated. The sign of $k_z \gtrless 0$ then agrees with the double sign introduced in (1) and (6).

We have argued that (13) is a line integral along a circle. Orthographic projection of this circle into the xy plane yields an ellipse. We now determine a parameterization of this ellipse. From (12) we read off the Laue diffraction condition

$$\mathbf{k}\hat{\mathbf{u}} = \pm\tau, \tag{18}$$

which defines the plane to be intersected with the unit sphere. We divide both sides by k and denote the Bragg angle of untilted crystallites as

$$\theta_{\mathrm{B}} := \arcsin(\tau/k). \tag{19}$$

From here on it is convenient to abbreviate

$$\begin{aligned} c_{\mathbf{k}} &:= \cos\theta_{\mathbf{k}}, & c_{\mathrm{B}} &:= \cos\theta_{\mathrm{B}}, \\ s_{\mathbf{k}} &:= \sin\theta_{\mathbf{k}}, & s_{\mathrm{B}} &:= \sin\theta_{\mathrm{B}}. \end{aligned} \tag{20}$$

The scalar product in (18) can be worked out as

$$\hat{\mathbf{k}}\hat{\mathbf{u}} = \Big(R_{\mathbf{k}}^{-1}\hat{\mathbf{k}}\Big)\hat{\mathbf{v}} = c_{\mathbf{k}}\alpha \pm s_{\mathbf{k}}\sqrt{1 - \alpha^2 - \beta^2}. \tag{21}$$

By rearranging (18), squaring and rearranging again, we obtain the ellipse equation

$$s_{\mathbf{k}}^{-2}\big(\alpha \mp s_{\mathrm{B}}c_{\mathbf{k}}\big)^2 + \beta^2 = c_{\mathrm{B}}^2 \tag{22}$$

that must be obeyed by diffracting block orientations. Resolving for α as a function of β^2, we obtain two solutions:

$$\begin{aligned} \alpha_{\mathbf{k}1}\big(\beta^2\big) &= \pm s_{\mathrm{B}}c_{\mathbf{k}} \mp s_{\mathbf{k}}\sqrt{c_{\mathrm{B}}^2 - \beta^2}, \\ \alpha_{\mathbf{k}2}\big(\beta^2\big) &= \pm s_{\mathrm{B}}c_{\mathbf{k}} \pm s_{\mathbf{k}}\sqrt{c_{\mathrm{B}}^2 - \beta^2}. \end{aligned} \tag{23}$$

The delta function from (12) can be linearized in α as

$$\delta(\mathbf{k}\hat{\mathbf{u}} \pm \tau) = \sum_{b=1}^{2}\frac{|s_{\mathrm{B}} \mp c_{\mathbf{k}}\alpha_{\mathbf{k}b}(\beta^2)|}{ks_{\mathbf{k}}\sqrt{c_{\mathrm{B}}^2 - \beta^2}}\delta\big(\alpha - \alpha_{\mathbf{k}b}(\beta^2)\big). \tag{24}$$

The α integration in the orientational average (13) can now be carried out, leaving us as intended with a one-dimensional integral

$$\begin{aligned} \mu(\mathbf{k}', \mathbf{k}) = \bar{\mu}\sum_{b}\int_{-c_{\mathrm{B}}}^{+c_{\mathrm{B}}} \mathrm{d}\beta\, W\big(\hat{\mathbf{u}}_{\mathbf{k}b}(\beta)\big)h_{\mathbf{k}b}\big(\beta^2\big) \\ \times\,\delta^3\big(\mathbf{k}' - \mathbf{k} \pm 2\tau\hat{\mathbf{u}}_{\mathbf{k}b}(\beta)\big) \end{aligned} \tag{25}$$

with a prefactor (as in Sears, 1989, equation 5.2.71)

$$\bar{\mu} = \frac{P^4}{k^3\sin 2\theta_{\mathrm{B}}}, \tag{26}$$

with a new, β-dependent correction factor

$$h_{\mathbf{k}b}(\beta^2) := \frac{c_{\mathrm{B}}}{\sqrt{c_{\mathrm{B}}^2 - \beta^2}}\frac{|s_{\mathrm{B}} \mp c_{\mathbf{k}}\alpha_{\mathbf{k}b}(\beta^2)|}{s_{\mathbf{k}}}, \tag{27}$$

and with the diffracting-block orientation

$$\hat{\mathbf{u}}_{\mathbf{k}b}(\beta) := R_{\mathbf{k}}\hat{\mathbf{v}}\big(\alpha_{\mathbf{k}b}(\beta^2), \beta\big). \tag{28}$$

From here on, the parameters τ, P and k will no longer appear separately as they only influence particle trajectories through the combined forms θ_{B} and $\bar{\mu}$.

2.3. Model transfer function

Equation (25) contains a line integral along an ellipse. Fig. 2 shows this ellipse for different values of $\theta_{\mathbf{k}} = \theta_{\mathrm{B}}$. It also shows the region where $W(\hat{\mathbf{u}})$ is substantially nonzero for a realistically chosen $\eta = 0.025$. One sees that the branch $\alpha_{\mathbf{k}2}$ lies outside this region, except near backscattering ($\theta \to 0$, ellipse is almost a circle, with radius going to zero) and near grazing incidence ($\theta \to \pi/2$, ellipse is extremely eccentric). Henceforth we exclude these two special geometries and retain only

the branch $\alpha_1(\beta^2)$. Accordingly, we can omit the summation in (25). Furthermore, we will drop all indices b.

From here on, we assume that the distribution of block orientations is isotropic:

$$W(\hat{\mathbf{u}}) = G(\alpha)G(\beta), \tag{29}$$

where G is an even normalized one-dimensional distribution function truncated at $\pm c_\mathrm{B}$. Accordingly, we can send the integration limits in (25) to $\pm\infty$. With these choices, (25) takes the form

$$\mu(\mathbf{k}', \mathbf{k}) = \bar{\mu} \int \mathrm{d}\beta G(\beta) G\big(\alpha_{\mathbf{k}}(\beta^2)\big) h_{\mathbf{k}}(\beta^2) \times \delta^3\big(\mathbf{k}' - \mathbf{k} \pm 2\tau\hat{\mathbf{u}}_{\mathbf{k}}(\beta)\big). \tag{30}$$

This equation constitutes our mathematical model of a Bragg reflection by a thin mosaic layer.

2.4. Analytical approximations

The $\mathbf{k}'$ integral over (30) is trivial and yields an expression for the lineic Bragg reflectivity

$$\mu(\mathbf{k}) \simeq \bar{\mu} \int \mathrm{d}\beta G(\beta) G\big(\alpha_{\mathbf{k}}(\beta^2)\big) h_{\mathbf{k}}(\beta^2). \tag{31}$$

To derive systematic approximations for (30) and (31), we need expansions of $\alpha_{\mathbf{k}}$ and $h_{\mathbf{k}}$ in β and in

$$\varepsilon := \theta - \theta_\mathrm{B}. \tag{32}$$

From (23), we find

$$\alpha_{\mathbf{k}}(\beta^2) = \mp\varepsilon \pm \frac{\tan\theta_\mathrm{B}}{2}\beta^2 + \mathcal{O}(\beta^4, \varepsilon\beta^2, \varepsilon^3). \tag{33}$$

From (27),

$$h_{\mathbf{k}}(\beta^2) = 1 - \frac{\tan^2\theta_\mathrm{B}}{2}\beta^2 + \mathcal{O}(\beta^4, \varepsilon\beta^2, \varepsilon^2). \tag{34}$$

For a first approximation to (31), we retain only the first term in (33) and (34), neglecting any β dependence. Geometrically, this means the original elliptical integration line is replaced by a vertical line that touches the ellipse at $\beta = 0$. Everthing except the normalized distribution $G(\beta)$ can be drawn in front of the integral, which then trivially yields unity. The result

$$\mu(\mathbf{k}) \simeq \bar{\mu} G(\varepsilon) \tag{35}$$

is known [equation (2)] from the Darwin–Hamilton approximation, which imposes $\beta = 0$ by neglecting out-of-plane scattering from the beginning.

With a little extra effort we can do better. To make the vertical line representative not just for in-plane scattering, but for the average of β^2 within the region of interest defined by the distribution W, we should shift it horizontally from $\alpha_{\mathbf{k}}(0)$ to a slightly larger value of α. Let us write $\langle\ldots\rangle$ for an average under the distribution $G(\beta)$, and apply the pre-averaging

$$\Big\langle h_{\mathbf{k}}(\beta^2) G\big(\alpha_{\mathbf{k}}(\beta^2)\big)\Big\rangle \simeq h_{\mathbf{k}}\Big(\langle\beta^2\rangle\Big) G\Big(\alpha_{\mathbf{k}}\big(\langle\beta^2\rangle\big)\Big). \tag{36}$$

Using the expansions (31) and (33) up to the order β^2 and writing η for the standard deviation of G, the reflectivity becomes

$$\mu(\mathbf{k}) \simeq \bar{\mu}\left(1 - \frac{\tan^2\theta_\mathrm{B}}{2}\eta^2\right) G\left(\varepsilon - \frac{\tan\theta_\mathrm{B}}{2}\eta^2\right). \tag{37}$$

Compared with (35), this predicts a reduction of intensity and a shift of the effective Bragg angle of the mosaic. Being of quadratic order in η, these are rather small corrections except in the limit $\theta_\mathrm{B} \to \pi/2$ where $\tan\theta_\mathrm{B}$ diverges – but the case of near backscattering needs special consideration anyway and is out of the scope of this work.

2.5. Numerical quadrature

For all numerical work in this paper we choose a mosaic spread parameter of $\eta = 0.025$. In terms of the block tilt angles $\arcsin\alpha$ or $\arcsin\beta$, it corresponds to a full width at half

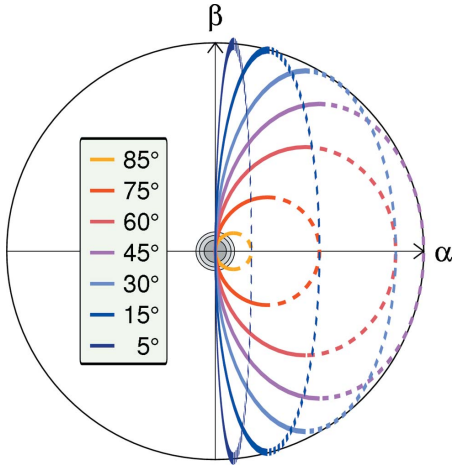

Figure 2
Orthographic projection of block normals $\hat{\mathbf{u}}$ into the xy plane (parallel to the surface of the mosaic slab). The scales α, β run from -1 to $+1$. The grey shaded circles in the centre illustrate a Gaussian distribution of block orientations, $W(\hat{\mathbf{u}})$, with $\eta = 0.025$. They contain 90, 99 and 99.9% of all blocks. The coloured ellipses (22), plotted for different angles $\theta = \theta_\mathrm{B}$, show which block orientations fulfil the diffraction condition (18). For each ellipse, the left branch (solid line) is given by $\alpha_{\mathbf{k}1}(\beta^2)$, the right branch (dashed) by $\alpha_{\mathbf{k}2}(\beta^2)$.

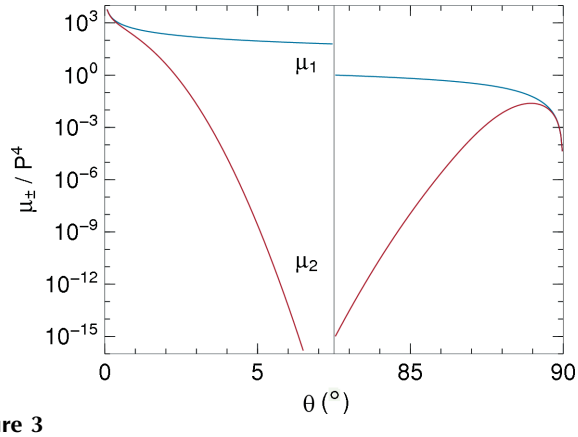

Figure 3
Contributions of the two ellipse branches (23) to the orientationally averaged Bragg reflectivity $\mu(\mathbf{k})$ as a function of the angle $\theta = \theta_\mathrm{B}$. Except near backscattering and near grazing incidence, the $b = 2$ branch contributes almost nothing.

maximum of 3.37°. This is a realistic value for pyrolytic graphite crystals used in special neutron optical applications, as mentioned in §1. Furthermore, we choose G to be a Gaussian truncated at $\pm\min(5\eta, c_B)$. For the quadrature of β integrals we use non-adaptive 61-point Gauss–Kronrod integration with a required relative accuracy of 10^{-8} (Galassi *et al.*, 2013).

Fig. 3 shows the contributions of the two ellipse branches $\alpha_{\mathbf{k}b}(\beta^2)$ to the orientationally averaged Bragg reflectivity $\mu(\mathbf{k})$, determined by numerical integration of (31), as a function of $\theta = \theta_B$. As expected, the $b = 2$ branch contributes almost nothing, except near grazing incidence and near backscattering. In the following, we restrict the angles θ and θ_B to values between about 5 and 85°, where the $b = 2$ branch can be neglected for good. The figure shows that this introduces a relative error of less than 10^{-8}.

To assess the error of the analytical approximations from §2.4, we consider rocking curves, namely μ as a function of θ for fixed θ_B. We choose a rather large Bragg angle $\theta_B = 80°$ so that the integration-line ellipses, shown in Fig. 4, have considerable curvature on the scale set by η. Fig. 5 shows the resulting $\mu(\mathbf{k})$. As expected, the literature approximation (35) is slightly shifted when compared with the quadrature result. The pre-averaging approximation (37) agrees better with the quadrature result, though it slightly underestimates the wings of the rocking curve. For all practical purposes, it should be good enough. However, to avoid subtle normalization errors in our Monte Carlo simulations, we work throughout with the numerical quadrature, though this costs about a factor of five in overall computation time.

3. Analytical theory of multiple Bragg reflection

In this section, we study radiation propagation in a thick mosaic crystal by analytical means. The transfer function of a thin mosaic layer, obtained in §2.2, is used to formulate the exact transport equation of our physical model, generalizing the Darwin–Hamilton equations (§3.1). We expand the generalized Darwin–Hamilton equations into a recursion of inhomogenous differential equations, which are easily quadrated (§3.2). The evolution of wavevectors under multiple Bragg reflection can be studied independently of the z coordinate (§3.3); the azimuth angle φ performs a random walk on the unit circle (§3.4), whereas the polar coordinate θ is confined to a narrow band around θ_B (§3.5). To quantify the importance of this wavevector diffusion, we break down the reflectivity, computed in Darwin–Hamilton approximation, into contributions from different scattering orders (§3.6).

3.1. Generalized Darwin–Hamilton equations

For a realistic description of multiple Bragg reflections in a mosaic crystal we need to generalize the Darwin–Hamilton equations (1) by allowing for a wavenumber dependence of the currents $I_\pm$. We shall not care about lateral displacement of the multiply deflected beam, so that we need no other real-space coordinate than the depth z. We obtain a stationary Boltzmann equation system, the generalized Darwin–Hamilton equations

$$k_z \partial_z I_\pm(\mathbf{k}, z) = -\nu(\mathbf{k}) I_\pm(\mathbf{k}, z) + \int \mathrm{d}^3k' \mu(\mathbf{k}, \mathbf{k}') I_\mp(\mathbf{k}', z). \quad (38)$$

The attenuation coefficient is

$$\nu(\mathbf{k}) = \mu(\mathbf{k}) + \sigma, \quad (39)$$

with $\mu(\mathbf{k}) = \int \mathrm{d}^3k' \mu(\mathbf{k}, \mathbf{k}')$ as determined in §2, and with a $\mathbf{k}$-independent coefficient σ accounting for the other loss

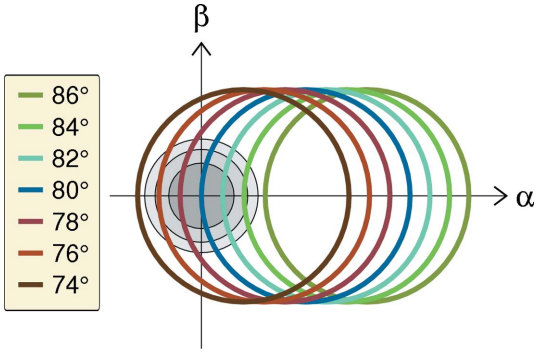

Figure 4
Block orientations in orthographic projection as in Fig. 2, zoomed into the region around $\alpha = \beta = 0$, where the orientational distribution $W(\hat{\mathbf{u}})$ is substantially nonzero (grey circles as in Fig. 2). The Bragg angle is fixed at $\theta_B = 80°$. The coloured ellipses show which block orientations fulfil the diffraction condition (18) for different incident angles θ from 74 to 86°.

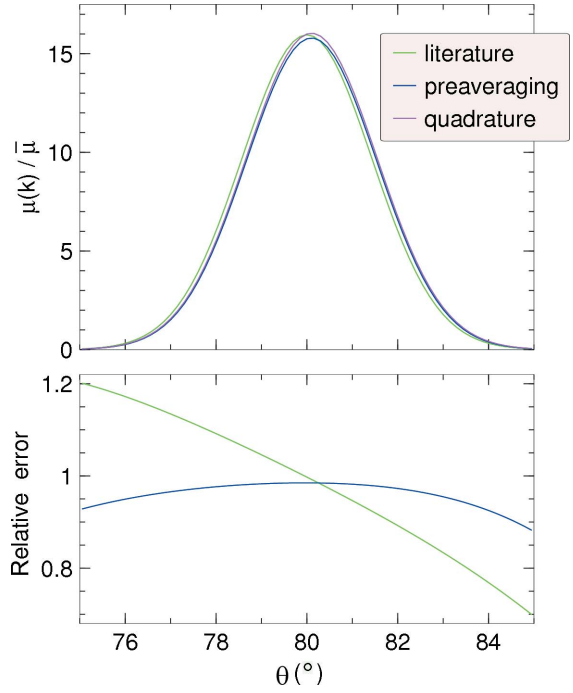

Figure 5
Orientationally averaged reflectivity $\mu(\mathbf{k})$ as a function of θ, at fixed Bragg angle $\theta_B = 80°$. The three colours correspond to the literature approximation [equation (35), green], to the pre-averaging approximation [equation (37), blue] and to numerical quadrature [equation (31), magenta]. The lower panel shows the relative error of the two analytical approximations with respect to the quadrature.

channels mentioned in §1. For a slab at $0 \le z \le d$, the boundary conditions are

$$\begin{aligned} I_+(\mathbf{k}, 0) &= I_\mathrm{i}(\mathbf{k}), \\ I_-(\mathbf{k}, d) &= 0, \end{aligned} \tag{40}$$

with a given incident current I_i. Note that primes are used differently than in §2: here we are concerned with scattering from $\mathbf{k}'$ towards $\mathbf{k}$. Using $\hat{k}_z = \pm \sin\theta_\mathbf{k}$, we introduce the reduced function

$$\tilde{\nu}(\mathbf{k}) := \nu(\mathbf{k})/\sin\theta_\mathbf{k}, \quad \tilde{\mu}(\mathbf{k}, \mathbf{k}') := \mu(\mathbf{k}, \mathbf{k}')/\sin\theta_\mathbf{k} \tag{41}$$

to rewrite (38) as

$$\big(\partial_{\pm z} + \tilde{\nu}(\mathbf{k})\big) I_\pm(\mathbf{k}, z) = \int \mathrm{d}^3k' \tilde{\mu}(\mathbf{k}, \mathbf{k}') I_\mp(\mathbf{k}', z). \tag{42}$$

3.2. Multi-reflection expansion

To get rid of the mutual coupling between I_+ and I_-, to gain more insight into trajectory statistics and to prepare for a Monte Carlo simulation, the generalized Darwin–Hamilton equations shall be expanded into a hierarchy of equations with unidirectional coupling:

$$\big(\partial_{\pm z} + \tilde{\nu}(\mathbf{k})\big) I_m(\mathbf{k}, z) = [m \ge 1] \int \mathrm{d}^3k' \tilde{\mu}(\mathbf{k}, \mathbf{k}') I_{m-1}(\mathbf{k}', z), \tag{43}$$

where $m = 0, 1, \ldots$ counts the number of Bragg reflections, the double sign is $\pm = (-)^m$, and the bracket in front of the integral is the Iverson–Knuth indicator function (Knuth, 1992; $[\mathcal{S}]$ is 1 if condition $\mathcal{S}$ is true, otherwise 0).

The boundary conditions (40) become

$$\begin{aligned} I_m(\mathbf{k}, 0) &= [m = 0] I_\mathrm{i}(\mathbf{k}), \ \text{ for even } m, \\ I_m(\mathbf{k}, d) &= 0, \ \text{ for odd } m. \end{aligned} \tag{44}$$

We assume the incoming current to be normalized to

$$\int \mathrm{d}^3k I_\mathrm{i}(\mathbf{k}) = 1, \tag{45}$$

so that the transmission of the slab is simply

$$T := \int \mathrm{d}^3k I_+(\mathbf{k}, d) = \sum_{m\,\mathrm{even}} \int \mathrm{d}^3k I_m(\mathbf{k}, d), \tag{46}$$

and the reflectivity is

$$R := \int \mathrm{d}^3k I_-(\mathbf{k}, 0) = \sum_{m\,\mathrm{odd}} \int \mathrm{d}^3k I_m(\mathbf{k}, 0). \tag{47}$$

The linear inhomogenous differential equation (43) with boundary conditions (44) is solved in the standard way up to quadrature. For $m = 0$,

$$I_0(\mathbf{k}, z) = \exp[-\tilde{\nu}(\mathbf{k}) z] I_\mathrm{i}(\mathbf{k}), \tag{48}$$

else

$$I_m(\mathbf{k}, z) = \int \mathrm{d}^3k' \int \mathrm{d}\zeta \tilde{\mu}(\mathbf{k}, \mathbf{k}') \Lambda_\pm(\mathbf{k}, z, \zeta) I_{m-1}(\mathbf{k}', \zeta), \tag{49}$$

with the kernel $\Lambda_\pm$ defined by

$$\begin{aligned} \Lambda_+(\mathbf{k}, z, \zeta) &= [0 \le \zeta \le z] \exp[-\tilde{\nu}(\mathbf{k})(z - \zeta)], \\ \Lambda_-(\mathbf{k}, z, \zeta) &= [z \le \zeta \le d] \exp[+\tilde{\nu}(\mathbf{k})(z - \zeta)]. \end{aligned} \tag{50}$$

Iterating (49), we obtain a closed solution

$$\begin{aligned} I_m(\mathbf{k}_m, z_m) = \prod_{j=0}^{m-1} \int \mathrm{d}z_j \int \mathrm{d}^3k_j \Lambda_{(-)^{j+1}}\big(\mathbf{k}_j, z_{j+1}, z_j\big) \\ \times \mu\big(\mathbf{k}_{j+1}, \mathbf{k}_j\big) I_0\big(\mathbf{k}_0, z_0\big). \end{aligned} \tag{51}$$

This can be rearranged as

$$\begin{aligned} I_m\big(\mathbf{k}_m, z_m\big) = \prod_{j=0}^{m-1} \left\{ \int \mathrm{d}z_j \Lambda_{(-)^{j+1}}\big(\mathbf{k}_j, z_{j+1}, z_j\big) \right\} \\ \times \prod_{j=0}^{m-1} \left\{ \int \mathrm{d}^3k_j \mu\big(\mathbf{k}_{j+1}, \mathbf{k}_j\big) \right\} I_0\big(\mathbf{k}_0, z_0\big), \end{aligned} \tag{52}$$

which means that the spread of wavevectors can be studied independently of the real-space coordinate z. In contrast, the penetration of real space depends on wavevectors. We therefore start the investigation of (52) with a z-independent study of wavevector diffusion.

3.3. Wavevector evolution

The z-independent part of (52),

$$J_m(\mathbf{k}_m) = \prod_{j=0}^{m-1} \left\{ \int \mathrm{d}^3k_j \mu(\mathbf{k}_{j+1}, \mathbf{k}_j) \right\} J_0(\mathbf{k}_0), \tag{53}$$

describes the evolution of wavevectors under multiple forth and back reflections inside an infinitely thick mosaic crystal. Introducing two more abbreviations,

$$\Gamma_j(\beta) := \bar{\mu} G(\beta) G\Big(\alpha_{\mathbf{k}_j}(\beta^2)\Big) h_{\mathbf{k}_j}(\beta^2) \tag{54}$$

and

$$\mathbf{q}_j(\beta) := \mp 2\tau \hat{\mathbf{u}}_{\mathbf{k}_j}(\beta) \tag{55}$$

with the double sign $\pm := (-)^{j+1}$, we can write the transfer function (30) as

$$\mu\big(\mathbf{k}_{j+1}, \mathbf{k}_j\big) = \int \mathrm{d}\beta \Gamma_j(\beta) \delta^3\big(\mathbf{k}_{j+1} - \mathbf{k}_j - \mathbf{q}_j(\beta)\big). \tag{56}$$

Carrying out one $\mathbf{k}$ integration,

$$J_{j+1}\big(\mathbf{k}_{j+1}\big) = \int \mathrm{d}\beta \Gamma_j(\beta) J_j\big(\mathbf{k}_j + \mathbf{q}_j(\beta)\big), \tag{57}$$

and iterating it yields

$$J_m(\mathbf{k}_m) = \prod_{j=0}^{m-1} \int \mathrm{d}\beta_j \Gamma_j\big(\beta_j\big) J_0\left(\mathbf{k}_m - \sum_{i=0}^{m-1} \mathbf{q}_i\big(\beta_j\big)\right). \tag{58}$$

This allows for a straightforward interpretation in Monte Carlo terms: at each reflection j, a random variable β_j is drawn from the distribution $\Gamma_j(\beta_j)$. The wavevector after m reflections is then obtained as the aggregated random variable

$$\mathbf{k}_m = \mathbf{k}_0 + \sum_{j=0}^{m-1} \mathbf{q}_j(\beta_j). \tag{59}$$

To investigate this random process, we start again from a single reflection:

$$R_{\mathbf{k}_j}^{-1}(\mathbf{k}_{j+1} - \mathbf{k}_j) = \mp 2\tau\hat{\mathbf{v}}\big(\alpha_{\mathbf{k}_j}(\beta_j^2), \beta_j\big). \tag{60}$$

Using polar coordinates (14), expanding the left-hand side of (60) to first order in $\Delta\theta$ and $\Delta\varphi$, the right-hand side to first order in α and β, and approximating $\theta \doteq \theta_B$ on the right-hand side, we find for the azimuth angle

$$\varphi_{j+1} - \varphi_j \doteq \mp 2\tan\theta_B \beta_j, \tag{61}$$

and for the polar angle

$$\theta_{j+1} - \theta_j \doteq \pm 2\alpha_{\mathbf{k}}(\beta_j^2). \tag{62}$$

3.4. Azimuth angle: random walk on the unit circle

Let us first study the evolution of φ. The difference equation (61) allows straightforward summation,

$$\varphi_m \doteq \varphi_0 - 2\tan\theta_B \sum_{j=0}^{m-1} (-)^j \beta_j. \tag{63}$$

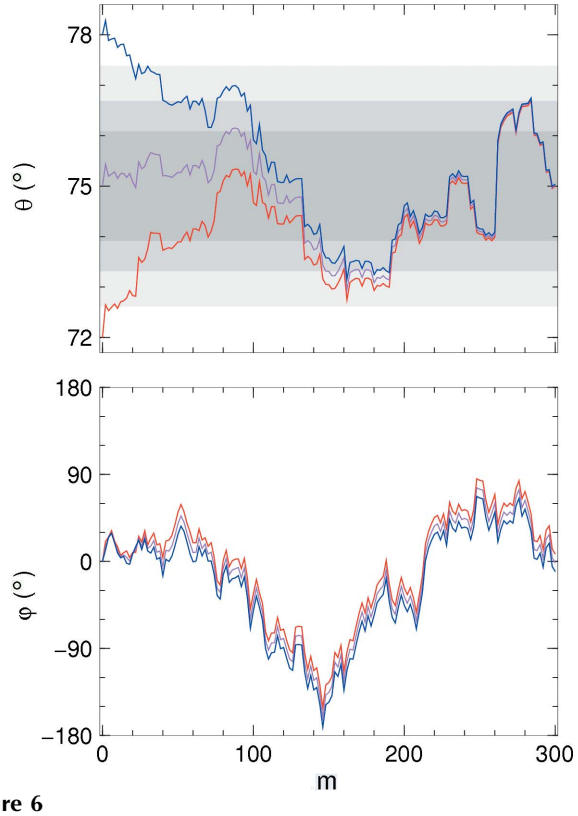

Figure 6
Spherical coordinates θ_m and φ_m of wavevectors $\mathbf{k}_m$ for even numbers of reflections m, from three Bragg-only simulation runs with different starting vectors $\mathbf{k}_0$, but with equal sequences of random-drawn orientations β_m of the reflecting crystalline blocks. The grey θ bands show regions where the Bragg reflectivity μ amounts at least 75, 50 and 25% of the maximum value attained at $\theta = \theta_B$.

The alternating sign is inconsequential since the β_j are drawn from a symmetric distribution. Equation (63) describes a standard random walk with mean $\langle\varphi_m\rangle \doteq 0$ and variance $\langle\varphi_m^2\rangle \doteq 4m\tan^2\theta_B\eta^2$.

For verification of this first-order analysis, Fig. 6 (lower panel) shows random walks simulated according to (60), hence without any approximations beyond our constitutive model (30). Three graphs, generated with identical random-number sequences but different starting values θ_0, evolve in parallel. This demonstrates that terms in ε (32), neglected in (61), have little importance so that the description of φ evolution as a simple, θ-independent random walk on the unit circle is accurate enough for all practical purposes.

3.5. Polar angle: confined random walk

To study the evolution of the polar angle (62), we express the θ through ε (32) and use the α expansion (33):

$$\varepsilon_{j+1} = -\varepsilon_j - \tan\theta_B\big(\varepsilon_j^2 + \beta_j^2\big). \tag{64}$$

The leading term $-\varepsilon$ implies a zigzag walk of θ around θ_B, which is of little consequence since $\mu(\mathbf{k})$ is in good approximation with an even function of ε. To get rid of the zigzag, we consider the combined effect of one forth and one back reflection. Iterating (64) once, we get

$$\varepsilon_{j+2} = \varepsilon_j + \tan\theta_B\big(\beta_j^2 - \beta_{j+1}^2\big) - 2\tan^2\theta_B\big(\varepsilon_j^2 + \beta_{j+1}^2\big)\varepsilon_j. \tag{65}$$

If there were only the first and the second term, this would be a symmetric random walk, with variance of the order η^4 in contrast to the order of η^2 for the φ walk. The third term, however, has always the sign of $-\varepsilon$. It is thus a restoring force, and has two effects: after a sufficient number of iterations, the θ_m value depends less and less on the initial value. This can be clearly seen in Fig. 6 (upper panel). And in the long run, the restoring force confines θ_m to a band around θ_B.

To estimate the width of this band, we need to investigate (65) closer. To deal with the first parenthesis, we write $\zeta := \beta_j^2 - \beta_{j+1}^2 = (\beta_j - \beta_{j+1})(\beta_j + \beta_{j+1})$. The two factors are independent normal-distributed random variables, and so is ζ, with $\langle\zeta\rangle = 0$ and $\langle\zeta_k\zeta_l\rangle = 4\eta^2[k = l]$. Pre-averaging the last parenthesis in (65), we obtain

$$\varepsilon_{j+2} - \varepsilon_j = \tan\theta_B\zeta - 2\tan^2\theta_B\big(\langle\varepsilon^2\rangle + \eta^2\big)\varepsilon. \tag{66}$$

This is a discrete Langevin equation of the form

$$\Delta\varepsilon = a\zeta - b\varepsilon, \tag{67}$$

solved by

$$\varepsilon_{2n} = \frac{a}{1-b}\sum_{k=-\infty}^{n-1}(1-b)^{n-k}\zeta_k. \tag{68}$$

The variance is

$$\big\langle\varepsilon^2\big\rangle = \frac{a^2}{2b - b^2}4\eta^2. \tag{69}$$

Anticipating $b \ll 1$, we obtain

$$\langle\varepsilon^2\rangle = \frac{2a^2\eta^2}{b} = \frac{\eta^2}{\langle\varepsilon^2\rangle + \eta^2}, \tag{70}$$

where the factors $\tan\theta_B$ of (66) have miraculously cancelled. The solution of this quadratic equation involves the golden ratio,

$$\langle\varepsilon^2\rangle = \frac{\sqrt{5}-1}{2}\eta^2. \tag{71}$$

Fig. 7 shows values of $\mathbf{k}_m$, generated in one hundred Monte Carlo runs, in orthographic projection. With increasing m, the random walk in φ_m causes the $\mathbf{k}_m$ to loose memory of the incoming direction and to be distributed around an entire circle. In contrast, the θ_m remain confined to a narrow band. This confirms that our analysis, based on expansions in ε and β, captures the essence of the wavevector diffusion during multiple forth and back reflections.

3.6. Reflected intensity by reflection order

To assess the effect of wavevector diffusion upon the reflected radiation, we need to know the partial currents

$$R_m = \int \mathrm{d}^3k I_m(\mathbf{k}, 0) \tag{72}$$

as a function of reflection order m (where m is odd). We consider a semi-infinite crystal ($d \to \infty$). This provides a worst-case estimate since the relative importance of multiple reflections increases with increasing crystal thickness.

We go back to the Darwin–Hamilton approximation, which means no out-of-plane scattering, $\theta = \text{const}$, and therefore also $\mu(\mathbf{k}) = \text{const}$ and $\nu(\mathbf{k}) = \text{const}$. The kernel $\Lambda_\pm$ (50) then loses its $\mathbf{k}$ dependence, and the iterated integration (52) can be carried out algebraically. This is so interesting that it has been published separately (Wuttke, 2014). The result is

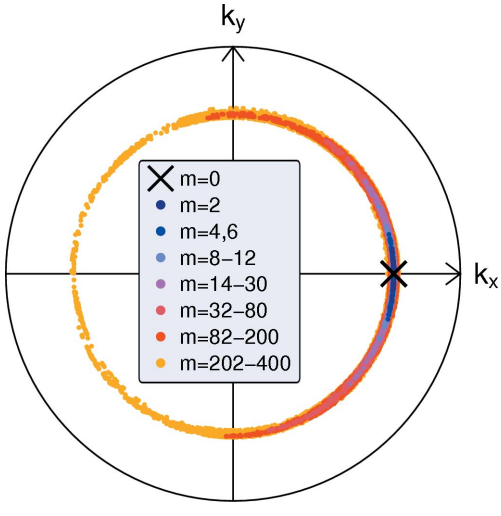

Figure 7
Orthographic projection of wavevectors $\mathbf{k}_m$ for even numbers of reflections m, from 100 different simulation runs. The coordinate scales k_x, k_y run from $-k$ to $+k$. The initial wavevector $\mathbf{k}_0$ lies in the xz plane, and has a polar angle that equals the Bragg angle, $\theta_0 = \theta_B = 45°$.

$$R_{2n+1} = C_n\left(\frac{\mu}{2\nu}\right)^{2n+1}, \tag{73}$$

with Catalan's numbers (*The On-Line Encyclopedia of Integer Sequences* (2014), sequence A000108)

$$C_n := \frac{(2n)!}{n!(n+1)!}. \tag{74}$$

The R_{2n+1} sum up to

$$R = \sum_{n=0}^{\infty} R_{2n+1} = \frac{\mu}{\sqrt{\nu^2-\mu^2}+\nu} \tag{75}$$

as expected from the $d \to \infty$ limit of Sears' (Sears, 1997) solution of the Darwin–Hamilton equations.

As (73) confirms, the relative importance of multiple reflections increases with decreasing probability of non-Bragg losses. To continue our worst-case estimate, we therefore consider the unphysical limiting case $\nu = \mu$, $R = 1$. The asymptote

$$R_{2n+1} \sim \frac{1}{2\sqrt{\pi}(n+1)^{3/2}} \tag{76}$$

is easily computed from Sterling's approximation. The intensity due to trajectories with $2n+1$ or more reflections is

$$\sum_{k=n}^{\infty} R_{2k+1} \simeq \int_{n-1/2}^{\infty} \mathrm{d}k R_{2k+1} \simeq \frac{1}{\sqrt{\pi}\sqrt{n+1/2}}. \tag{77}$$

Fig. 8 shows that it is a surprisingly good approximation even for the lowest n. Convergence of this curve is slow; there is a 10% contribution from trajectories with 63 and more Bragg reflections. However, as the figure also shows, this long tail disappears as soon as there is some non-Bragg attenuation. For $\mu = 0.95\nu$, no more than 1% of the particles reflected by the mosaic undergo more than 25 Bragg reflections.

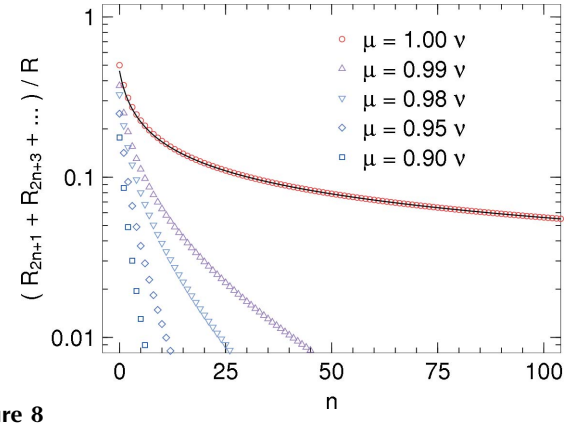

Figure 8
Relative contributions to the radiation reflected by a semi-infinite mosaic crystal from trajectories with at least $2n+1$ Bragg reflections. Computed in Darwin–Hamilton approximation by summing (73). Different symbols for different values of μ/ν. The solid line is the asymptote (77) for $\mu = \nu$.

4. Monte Carlo simulation

In this paper, analytical methods prevail, and only a few Monte Carlo results are shown to confirm and complement analytical results. However, in future applications of the generalized Darwin–Hamilton equations for the design of optical components, Monte Carlo simulations will become indispensable. As a starting point for such work, the code developed here is made available online (§4.1). Since the algorithm is mostly standard, only a few explanations are in order, concerning the propagation in real space (§4.2) and the random drawing of wavenumbers (§4.3).

4.1. Simulation code

The source code of the multi-reflection simulation software developed for this work is released under the *GNU* General Public License, and has been deposited as supporting information.[1] It is published as used in the latest simulations performed for this paper, without any cleaning up, without any pretension of showing particularly good coding practice and without much optimization. It is published for only two reasons: to provide a complete documentation of the present work and to offer a starting point for future developments.

The code is written in the C++ programming language. A random number generator with dedicated support for parallel processing (Bauke & Mertens, 2007; Bauke, 2014) allows the simulation to run in multi-processor mode.

4.2. Simulating real-space trajectories

There is a good rule in Monte Carlo simulation to do analytically whatever can be done analytically. From equations (50) and (52) it appears that the entire z dependence of our currents is a strong candidate for a fully analytical treatment. For a given wavevector sequence $\mathbf{k}_j$, iterated z integrals over different exponential function yield sums of exponential functions, which in principle should allow for an algebraic computation. However, the small variations of the reflection coefficient $\tilde{\nu}(\mathbf{k}_j)$ cause problems with nearly cancelling differences. In fact, in the special case of constant $\tilde{\nu}$, iterated integration does not reproduce exponential kernels, but an exponential times a polynomial (Wuttke, 2014). Therefore, an analytical treatment of the realistic problem with finite d and $\mu < \nu$ is not viable.

Instead, a standard algorithm from neutron transport simulations (*e.g.* Spanier & Gelbard, 1969; Copley, 1974) is employed: at each Bragg reflection, the contribution to the transmitted (46) or reflected (47) score is computed. The particle is forbidden to leave the slab; instead, its stochastical weight is adjusted for the escape probability. To terminate simulated trajectories without bias, Russian roulette is played.

In the case of a very thick slab we run into a numeric problem that is well known from shielding calculations (Kahn, 1950; Leimdörfer, 1964): only few trajectories penetrate the slab deeply enough to allow for an accurate estimation of logarithmically small transmissions T, unless appropriate variance-reducing techniques are applied. In our context, we expect little interest in the residual transmission of excessively thick crystals; we concentrate on the reflectivity, which can be simulated in straightforward ways.

4.3. Wavevector drawing

Recently, Hennig *et al.* (2011) have combined Sears' in-plane multiple-reflection intensity with an out-of-plane single-reflection random drawing of deflected wavevectors. With the additional complication of a Galilei transform into the moving frame of a rotating-crystal chopper, they arrived at a rather involved formalism.

Based on the preceding investigation of the mosaic transfer function (30), we can derive a much simpler prescription for drawing reflected wavevectors. For each simulated Bragg reflection we need to draw a representative block orientation $\hat{\mathbf{u}}$. The outgoing wavevector is then determined by (5). The pertinent distribution of $\hat{\mathbf{u}}$ is a conditional probability: we consider a thin layer of the mosaic crystal and ask for the probability that scattering is caused by a block of orientation $\hat{\mathbf{u}}$ under the condition that scattering takes place at all. This conditional probability can be computed using Bayes' theorem:

$$P(\hat{\mathbf{u}}|\mathrm{sca}) = \frac{P(\mathrm{sca}|\hat{\mathbf{u}})W(\hat{\mathbf{u}})}{\int \mathrm{d}\hat{\mathbf{u}}'\, P(\mathrm{sca}|\hat{\mathbf{u}}')W(\hat{\mathbf{u}}')}, \tag{78}$$

with $P(\mathrm{sca}|\hat{\mathbf{u}}) \propto \mu_{\hat{\mathbf{u}}}(\mathbf{k})$ given by the $\mathbf{k}'$ integral of (12). As in §2.2, $\hat{\mathbf{u}}$ is parameterized by α and β. Excluding the second ellipse branch, we can conclude from (24) that α is uniquely determined by β as $\alpha_{\mathbf{k}}(\beta^2)$, and that β is distributed as

$$P(\beta|\mathrm{sca}) = \frac{h_{\mathbf{k}}(\beta^2)G\big(\alpha_{\mathbf{k}}(\beta^2)\big)G(\beta)}{\int \mathrm{d}\beta'\, h_{\mathbf{k}}(\beta'^2)G\big(\alpha_{\mathbf{k}}(\beta'^2)\big)G(\beta')}. \tag{79}$$

In the β range where $G(\beta)$ is substantially nonzero, the factors $h_{\mathbf{k}}(\beta^2)$ and $G\big(\alpha_{\mathbf{k}}(\beta^2)\big)$ are slowly varying functions of β. To simulate a scattering event in a simple and efficient way, we just draw β from $G(\beta)$. All other factors of (79) are taken into account as stochastical weight of the scattered particle.

5. Simulational *vs* analytical results

Combining Monte Carlo simulations with analytical results, the following questions can now be answered. How does out-of-plane scattering affect the reflectivity of a thick crystallite (§5.1)? How does it modify rocking curves (§5.2)? How do different reflection orders contribute to the total reflectivity (§5.3)? And what is the orientational distribution of the reflected radiation (§5.4)?

5.1. Mosaic reflectivity

In the following, we investigate the reflectivity of a mosaic slab as a function of the Bragg angle θ_{B} and the incident angle θ_0. To avoid results being dominated by the trivial variation of path lengths with $1/\sin\theta_{\mathbf{k}}$, we parameterize reflectivity

[1] The source code is available from the IUCr electronic archive (reference: SC5071).

and attenuation in terms of $\tilde{\mu}_0 := \bar{\mu}G(0)/\sin\theta_0$, and $\tilde{\sigma}_0 := \sigma/\sin\theta_0$.

In the Darwin–Hamilton approximation with $\theta_0 = \theta_B$, the index 0 can be dropped since reflections do not change $\tilde{\mu}$ and $\tilde{\sigma}$. Reflectivity and transmission computed by Sears (1997) reduce to

$$R_0 = \frac{\tilde{\mu}\sin h\tilde{\rho}}{\tilde{\rho}\cos h\tilde{\rho} + \tilde{\nu}\sin h\tilde{\rho}},$$
$$T_0 = \frac{\tilde{\rho}}{\tilde{\rho}\cos h\tilde{\mu} + \tilde{\rho}\sin h\tilde{\mu}}, \quad (80)$$

with

$$\tilde{\rho} := \sqrt{\tilde{\nu}^2 - \tilde{\mu}^2}. \quad (81)$$

The generalized Darwin–Hamilton equations allow for fluctuations of θ, and in consequence also of μ and ν. We now enquire whether these fluctuations result in a noticeable change of R and T.

In the limit $d \to 0$, the reflectivity $R \doteq \tilde{\mu}_0 d$ is not influenced by multiple Bragg reflections. In the opposite limit $d \to \infty$, it is just $R = 1$ unless there is some non-Bragg attenuation. Therefore, effects of out-of-plane reflections are expected to be most important for intermediate slab thicknesses, and when there is substantial concurrence between scattering and absorption. Furthermore, since various effects of out-of-plane scattering go with $\tan\theta_B$ [(37), (63) and (66)], we expect deviations from the Sears solution to be largest for $\theta_B \to \pi/2$. All this is confirmed by simulations. Fig. 9 shows R as a function of $\theta_0 = \theta_B$ for different combinations of $\tilde{\mu}_0 d$ and $\tilde{\sigma}_0 d$ chosen to yield the same Sears reflectivity of 0.5. The true reflectivity, determined by Monte Carlo integration of the generalized Darwin–Hamilton equations, shows small but systematic deviations from the Sears solution that increase with increasing θ and with increasing σ/μ.

The increase of R with increasing θ_B contrasts with (37), which predicts a *decrease* of $\mu(\mathbf{k})$ for increasing $\tan\theta_B$. This shows that the inaccuracy of the conventional Darwin–Hamilton equations is not primarily due to the in-plane approximation for the thin-layer reflectivity $\mu(\mathbf{k})$, but to the neglect of θ fluctuations in multiple reflections.

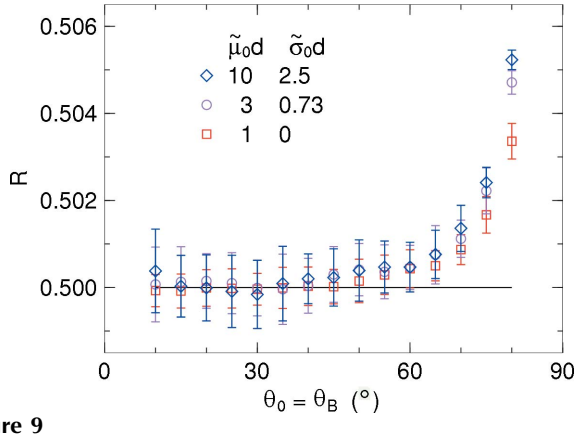

Figure 9
Reflectivity of a mosaic slab of thickness d as a function of Bragg angle θ_B, with the incident collimated beam perfectly aligned to $\theta_0 = \theta_B$, for different combinations of reduced Bragg reflectivity $\tilde{\mu}_0$ and reduced non-Bragg attenuation coefficient $\tilde{\sigma}_0$ that all yield a Sears reflectivity of 0.500 (line).

5.2. Rocking curves

We now consider θ_0 scans at constant θ_B. The incoming beam is collimated, the mosaic slab is rotated around an axis perpendicular to the incoming beam direction and detectors cover enough solid angle to capture all transmitted or reflected intensity. Fig. 10 shows the reflected intensity R, the transmitted intensity T and the non-Bragg losses $1 - R - T$ as a function of θ_0 for two Bragg angles θ_B.

For $\theta_B = 45°$, Monte Carlo results, based on the generalized Darwin–Hamilton equations, deviate only little from Sears' solution of the conventional Darwin–Hamilton equations. Furthermore, the reflectivity curves can be fitted almost perfectly by a damped Gaussian, obtained by concatenating a

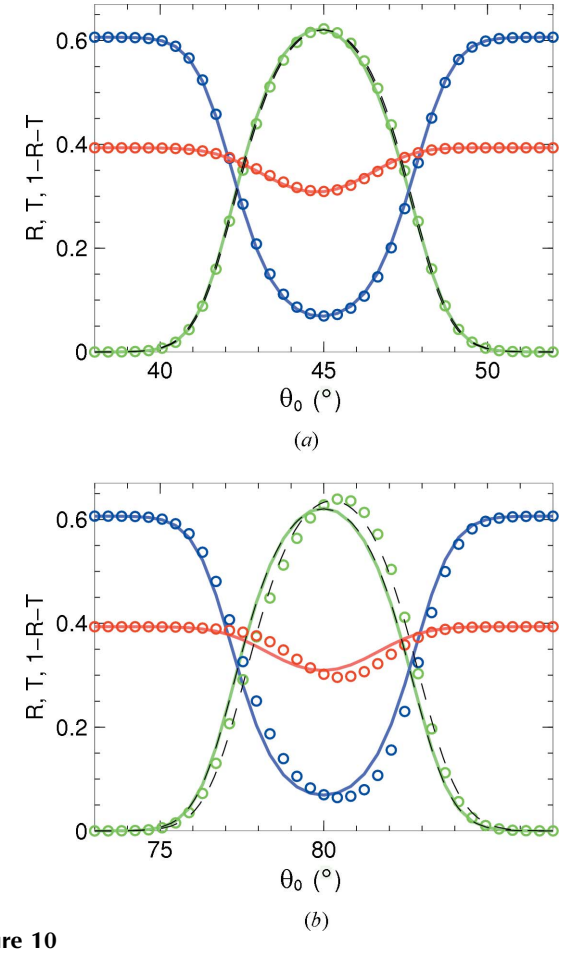

Figure 10
Reflectivity R (green), transmission T (blue) and non-Bragg losses $1 - R - T$ (red) in a mosaic slab with thickness d, thin-layer reflectivity $\tilde{\mu}_0 d = 4.5$, non-Bragg attenuation coefficient $\tilde{\sigma}_0 d = 0.5$, as a function of incident angle θ_0. The Bragg angle is (*a*) $\theta_B = 45°$, (*b*) $\theta_B = 80°$. Solid lines according to Sears' solution of the conventional (in-plane) Darwin–Hamilton equations. Circles from Monte Carlo integration of the generalized Darwin–Hamilton equations; error bars smaller than the symbols. Dashed lines: fits with a damped Gaussian as described in the text.

Gaussian [which can be justified by combining (35) with a small-d expansion of (80)] with the simplest description of saturation, $R \mapsto R/(1+R)$.

For $\theta_B = 80°$, on the other hand, there are noteworthy differences between the simulation results and Sears' solution. The maximum of the reflectivity curve is shifted from 80° to about 80.5°, and the maximum reflectivity is increased by about 3%. The damped Gaussian still fits Sears' solution, but no longer the simulated reflectivity; deviations highlight the asymmetry of the simulated reflectivity curve.

5.3. Reflection order statistics

In §3.6, we have discussed how different reflection orders contribute to the total reflectivity of a semi-infinite mosaic in Darwin–Hamilton approximation. For a more realistic estimation, we consider a slab of finite thickness and describe multiple reflections by the generalized Darwin–Hamilton equations. Fig. 11 shows Monte Carlo results for different slab thicknesses d, with constant attenuation ratio $\tilde{\sigma}/\tilde{\nu}_0 = 0.1$.

In the large-d, small-n limit, we find perfect agreement with the Darwin–Hamilton infinite-d asymptote (73). At large d and large n, deviations from this asymptote are due to out-of-plane wavevectors, which cause fluctuations in θ and thence in $\tilde{\mu}$ and $\tilde{\nu}$, whereas the finite value d is irrelevant. However, for not so large values of d the dependence of R_{2n+1} on d is dramatic; in this regime, the main shortcoming of the analytical model is not the confinement of wavevectors to a plane, but the choice of a semi-infinite crystal. In conclusion, (73) is reliable as a worst-case estimate of multiple-reflection effects and it provides realistic partial reflectivities in the case of relatively thick crystals, particularly for low reflection orders.

5.4. Orientational distribution

As Darwin anticipated, multiple reflections increase the orientational spread of the reflected radiation. We now quantify this spreading. We consider again a rather large angle $\theta_0 = \theta_B = 80°$ and a rather thick crystal ($\tilde{\nu}_0 d = 16$) for which we expect relatively important contributions from multiply reflected rays. On the other hand, to remain realistic, we assume 10% non-Bragg attenuation as we did in Fig. 11.

Fig. 12 shows the azimuth angle distribution of the reflected radiation. Up to reflection order $n \lesssim 7$, the partial distributions are almost perfectly predicted by combining the intensity per reflection order (73) with the random-walk variance derived from (63):

$$R_{2n+1}(\varphi) = C_n \left(\frac{\mu}{2\nu}\right)^{2n+1} \mathcal{G}\left(\varphi; \sqrt{4m}\tan\theta_B \eta\right), \qquad (82)$$

where $\mathcal{G}(x; s)$ is a Gaussian in x with standard deviation s. By summing (82) numerically, an excellent approximation to the total intensity distribution is obtained, which is a Gaussian with additional exponential wings. For the parameters chosen in the figure, the central Gaussian has a standard deviation of 18.2°, which is only 12% more than the standard deviation $2\tan\theta_B\eta = 16.2°$ of the single-reflection distribution as obtained from (63). About 5.8% of the total reflected intensity belongs to the non-Gaussian tails.

Fig. 13 shows the polar angle distribution as a function of $\varepsilon = \theta - \theta_B$. After the first Bragg reflection, ε must be negative [equation (64)]. It takes several reflections for this asymmetry to average out. For $n \gtrsim 10$, the θ distribution approaches a Gaussian with width as expected from (71). There is no simple functional approximation to the highly asymmetric total intensity distribution.

6. Conclusion

We have studied multiple Bragg reflection in a mosaic crystal. Following Darwin (1922), the mosaic is modelled as an assembly of randomly oriented thin perfect crystalline blocks. Past studies of radiation propagation in such a mosaic were based on the Darwin–Hamilton equations, which assume that wavevectors are confined to the scattering plane. To overcome this uncontrolled approximation, we have derived and solved generalized Darwin–Hamilton equations that include out-of-plane scattering.

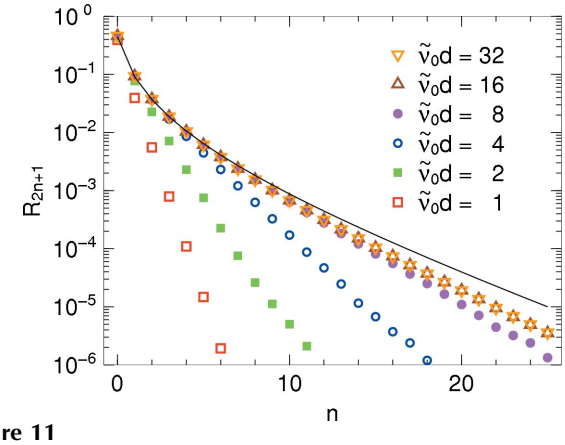

Figure 11
Partial reflectivity R_{2n+1} as a function of the reflection order $m = 2n+1$ for $\theta_0 = \theta_B = 80°$. Different symbols for different sample thickness; constant ratio $\tilde{\sigma}/\tilde{\nu}_0 = 0.1$. The black line shows R_{2n+1} in Darwin–Hamilton approximation for the limiting case $d \to \infty$ (73).

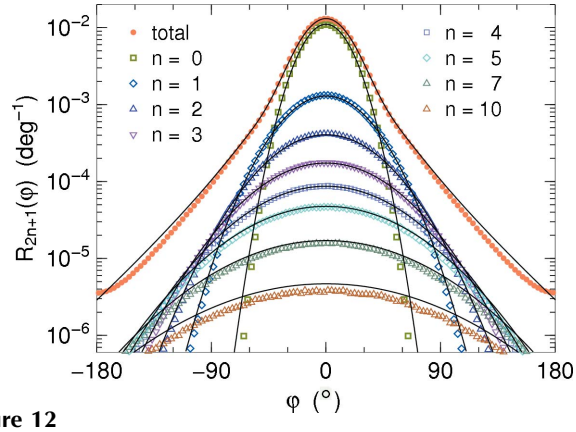

Figure 12
Azimuth angle distribution of reflected radiation and partial distributions by reflection order n for $\theta_0 = \theta_B = 80°$, $\tilde{\nu}_0 d = 16$, $\sigma/\nu = 0.1$. Solid lines show the analytical approximation (82).

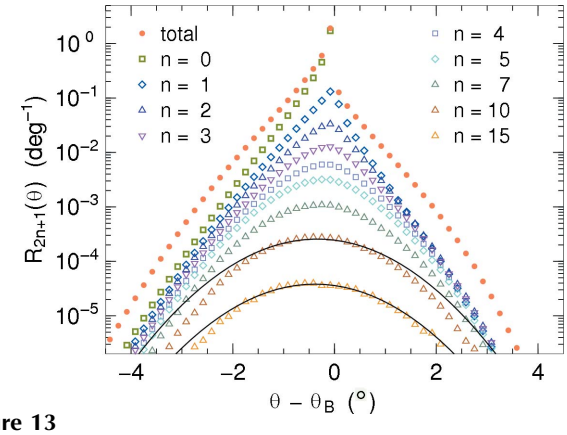

Figure 13
Polar angle distribution of reflected radiation, and partial distributions by reflection order n for the same parameters as in Fig. 12. Solid lines show a Gaussian with standard deviation 1.13° as expected for the limit $n \to \infty$ (71).

We studied a wide range of Bragg angles and incoming angles, excluding only the special cases of grazing incidence near backscattering. Since several effects of out-of-plane scattering go with $\tan\theta_B$ [(37), (63) and (66)], we mostly concentrated on a rather large Bragg angle of 80°. However, since the wavevector declination is $k_y/k = \cos\theta\sin\varphi$, the denominator cosine in $\tan\theta_B$ cancels, so that there is no physical singularity for $\theta_B \to 90°$.

In a zeroth approximation, one can combine reflectivities from Sears' (Sears, 1997) solution of the Darwin–Hamilton equations with the orientational distribution from single scattering, as Hennig *et al.* (2011) have done implicitly. In a first approximation, multiple reflection can be taken into account by combining the intensity per reflection order (73) with a random-walk description of the azimuth angle evolution (61). This matches the simulated distribution almost perfectly (Fig. 12). However, since no analytic approximation has been obtained for the highly asymmetric polar angle distribution (Fig. 13), Monte Carlo simulations remain indispensable.

The asymmetry of the θ distribution causes rocking curves to be shifted and skewed (Fig. 10). Of all results, this shift of the rocking curves is the most likely to admit experimental verification. In contrast, the tails of the φ distribution, though looking spectacular in a log plot (Fig. 12), would not provide a convincing proof of multiple-reflection effects: they could also result from non-Gaussian tails of the actual crystalline block orientation distribution. In reality, both effects probably combine. The right conclusion from Fig. 12 is therefore: To derive block orientation distributions from measured rocking curves, either use a very thin crystal sample or correct for multiple reflection.

References

Bacon, G. E. & Lowde, R. D. (1948). *Acta Cryst.* **1**, 303–314.
Bauke, H. (2014). *Tina's Random Number Generator Library*. http://numbercrunch.de.trng/.
Bauke, H. & Mertens, S. (2007). *Phys. Rev. E*, **75**, 066701.
Copley, J. R. D. (1974). *Comput. Phys. Commun.* **7**, 289–317.
Darwin, C. G. (1922). *Philos. Mag.* **43**, 800–822.
Galassi, M., Davies, J., Theiler, J., Gough, B., Jungman, G., Alken, P., Booth, M., Rossi, F. & Ulerich, R. (2013). *GNU Scientific Library Reference Manual*. http://www.gnu.org/software/gsl/manual.
Hamilton, W. C. (1957). *Acta Cryst.* **10**, 629–634.
Hennig, M., Frick, B. & Seydel, T. (2011). *J. Appl. Cryst.* **44**, 467–472.
Kahn, H. (1950). *Nucleonics*, **6**, 27–37.
Knuth, D. E. (1992). *Am. Math. Mon.* **99**, 403–422.
Leimdörfer, M. (1964). *Nukleonik*, **6**, 58–65.
Meyer, A., Dimeo, R. M., Gehring, P. M. & Neumann, D. A. (2003). *Rev. Sci. Instrum.* **74**, 2759–2777.
Sabine, T. M. (2004). *International Tables for Crystallography*, Vol. C, pp. 609–616. Dordrecht: Kluwer.
Schelten, J. & Alefeld, B. (1984). *Proceedings of the Workshop on Neutron Scattering Instrumentation for the SNQ*, Maria Laach, 3–5 Sept., edited by R. Scherm & H. Stiller, Vol. Jül-1954, p. 378. Berichte der Kernforschungsanlage Jülich.
Sears, V. F. (1989). *Neutron Optics.* Oxford University Press.
Sears, V. F. (1997). *Acta Cryst.* A**53**, 35–45.
Spanier, J. & Gelbard, E. M. (1969). *Monte Carlo Principles and Neutron Transport Problems.* Reading, MA: Addison-Wesley.
The On-Line Encyclopedia of Integer Sequences (2014). http://oeis.org/.
Werner, S. A. (1974). *J. Appl. Phys.* **45**, 3246–3254.
Wuttke, J. (2014). *J. Phys. A Math. Theor.* **47**, 215203.
Wuttke, J., Budwig, A., Drochner, M., Kammerling, H., Kayser, F.-J., Kleines, H., Ossovyi, V., Pardo, L. C., Prager, M., Richter, D., Schneider, G. J., Schneider, H. & Staringer, S. (2012). *Rev. Sci. Instrum.* **83**, 075109.
Zachariasen, W. H. (1945). *Theory of X-ray Diffraction in Crystals.* New York: Wiley.